*Desalination and Water Treatment*
www.deswater.com
doi: 10.5004/dwt.2023.29337

286 (2023) 205–216
February

# Photocatalytic treatment of Cr(VI) with $ZrO_2$ and application of by-products as ethane dehydrogenation catalyst

Jing Yang[a], Siyuan Yang[a], Jing Zhang[a], Jian He[b,*], Wei Jiang[b]

[a]*Sinopec Northwest Oilfield Branch, Urumqi 830000, P.R. China, emails: 365712163@qq.com (J. Yang), 125854377@qq.com (S. Yang), 10271575@qq.com (J. Zhang)*
[b]*School of Chemical Engineering, Sichuan University, Chengdu 610065, P.R. China, emails: jianhe@scu.edu.cn (J. He), weijiang@scu.edu.cn (W. Jiang)*

Received 13 July 2022; Accepted 29 January 2023

**ABSTRACT**

The recovery of Cr(VI) from the solution and the utilization of by-products are significant for wastewater treatment and environmental protection. In this study, the amorphous $ZrO_2$ was prepared using a solvothermal method and used to treat the wastewater containing Cr(VI). Amorphous $ZrO_2$ is effective for the photocatalytic reduction of Cr(VI). Without a sacrificial agent, 20 mL potassium dichromate solution (20 mg/L) is reduced to almost 0 mg/L within 10 min. Moreover, the by-products obtained from this process exhibit good performance in the catalytic dehydrogenation of ethane coupled with the reverse water–gas reaction. The maximum yield of ethylene is 12.9%, and the service life of the catalyst reached 160 min. Catalyst deactivation is caused by carbon deposition, and the deactivated catalyst is regenerated by roasting in the air. The feasibility of this green process is demonstrated, including the one-step photocatalytic reduction of Cr(VI) and utilization of the by-product as an ethane dehydrogenation catalyst.

*Keywords:* Amorphous $ZrO_2$; Cr(VI); Photocatalytic reduction; Ethane dehydrogenation

## 1. Introduction

The wide application of chromium in metallurgy [1,2], electroplating [3,4], tanning [5,6], and other industries has led to the generation of a large amount of chromium slag and chromium-containing wastewater. This wastewater originates primarily from chromium electroplating on the surface of industrial parts and chromium-containing tanning agents used in leather manufacturing. The manufacture of ceramics [7,8] and glass [9,10] also causes chromium pollution through the use of chromium-containing substances. The discharge of substandard chromium-containing wastewater and solid waste causes serious environmental pollution and threatens human life.

In water, the primary Cr species are Cr(III) and Cr(VI). Cr(VI) is stable in water and does not degrade. In nature, it exists predominantly in the free forms of $Cr_2O_7^{2-}$ [11], $CrO_4^{2-}$ [12], $H_2CrO_4$ [13], and $HCrO_4^-$ [14]. The pH of the solution determines the concentration distribution of each ion. Trace Cr(III) is beneficial to the human body, whereas Cr(VI) is very harmful because of its carcinogenicity [15]. Therefore, the chromium-containing wastewater should be discharged only after the chromium is degraded, such that the chromium ion concentration meets the discharge standard.

Current treatment techniques for Cr(VI) can be divided into direct removal [16,17] and chemical precipitation [18], and they primarily include chemical reduction precipitation [19,20], adsorption [21,22], ion exchange [23,24], biotechnology [25,26], electrochemistry [27,28] and photocatalytic reduction precipitation [29–31]. In the adsorption method, the adsorbent must be desorbed before recycling it in the treatment of chromium-containing wastewater. Hence, the

* Corresponding author.

recovery and utilization of chromium cannot be realized. As a result, adsorptive Cr removal has no industrial application prospects. In the treatment of chromium-containing wastewater by the ion exchange method, the wastewater needs to be filtered in advance, and the resin is easily polluted and loses its purification effect, resulting in the use of a large number of resins, which increases the cost. The microbial method offers the advantage of environment-friendliness. However, its problems of low degradation efficiency, high cost, and non-standard treatment also limit its application in industry.

The photocatalytic reduction treatment of Cr(VI) has the advantages of high efficiency [32], high removal rate [33], low toxicity of the by-products, energy savings, and economy. The principle of photocatalytic reduction is based on the photoelectric effect. Under the light, the electrons in the semiconductor valence band absorb photons and transition to the conduction band to produce photogenerated electron ($e^-$) and hole ($h^+$) pairs, which are transmitted to the semiconductor surface. The photoelectrons on the semiconductor surface reduce the metal ions that are adsorbed on the semiconductor surface to realize the degradation of Cr(VI). However, the photocatalytic reduction can only reduce Cr(VI) to water-soluble Cr(III), after which the pH is adjusted to precipitate Cr(III). The treatment process is complex, and the utilization value of chromium mud is low. Commonly used catalysts include $TiO_2$ [34,35], ZnO [36,37], and $Cu_2O$ [30,38,39].

In previous research [40], $ZrO_2$ prepared by the sol-gel method was used for the photocatalytic reduction of Cr(VI) in the deposition solution. As a catalyst, chromium exhibits good performance in ethane dehydrogenation. Therefore, an environmental-friendly route is proposed in this study. Herein, amorphous $ZrO_2$ was prepared. The Cr(VI) in an aqueous solution was deposited by one-step photocatalytic reduction. The by-product $Cr/ZrO_2$ was coupled with the reverse water gas reaction to catalyze ethane dehydrogenation.

The solvothermal method was used to prepare amorphous $ZrO_2$, and the one-step degradation of Cr(VI) in solution was investigated in this study. The photocatalytic performance and maximum Cr loading were investigated. The by-products were used to catalyze the oxidative dehydrogenation of ethane for clarifying the efficiency of amorphous $ZrO_2$ in the reduction of Cr(VI) and the mechanism of catalytic dehydrogenation of ethane.

## 2. Materials and method

### 2.1. Materials

The gases (ethane (99.99%), $CO_2$ (99.9%), and dry air) were purchased from the Chengdu Keyuan Gas Co., Ltd., (China). Zirconium *n*-butoxide, oleylamine, and ethylene mercaptan were purchased from Aladdin (China). Other reagents used in this study were purchased from Chengdu Kelong Chemical Co., Ltd., (China). All the reagents were analytically pure and were used without further purification.

### 2.2. Preparation of $ZrO_2$

In this process, zirconium *n*-butanol (1 mL) was dissolved in oleamine (5 mL) under continuous magnetic agitation. After stirring for 10 min, 1,2-ethyldimercaptan (5 mL) was dropped into the above solution and the mixed solution turned red immediately. The solution was evenly mixed by stirring, and the mixture was transferred to a high-pressure hydrothermal kettle. The reaction mixture was maintained at 200°C for 24 h. Subsequently, a white precipitate was obtained at the bottom of the container. The obtained precipitate was washed 10 times with ethanol and then 10 times with a mixture of n-hexane and ethanol (volume ratio of 1:6). Finally, the samples were freeze-dried under vacuum for 24 h, and then dried in an oven for 12 h at 60°C. The obtained amorphous $ZrO_2$ was labeled as a-$ZrO_2$. The $ZrO_2$ prepared with sol–gel method in a previous study was named s-$ZrO_2$. For details on the preparation process, please refer to the paper published previously by our group in 2018 [40].

### 2.3. Evaluation of the photocatalytic performance

A CEL-Lab500 photocatalytic reactor with a 500 W mercury lamp was used in this study. A filter was placed between the quartz tube and the lamp to ensure that only ultraviolet (UV) light reached the reaction tube. The photocatalyst (a-$ZrO_2$) was dispersed in a potassium dichromate solution, and the mixed solution was stirred in a dark environment for 60 min to achieve adsorption equilibrium. After the adsorption process, methanol (1 mL) was added to the solution as a hole scavenger, and then the mixed solution was irradiated with UV light. The absorbance of the solution was measured using a UV-1500PC spectrophotometer. The concentration of potassium dichromate solution could be determined according to Lambert–Beer's law.

### 2.4. Adsorption performance of the catalyst

First, a-$ZrO_2$ (0.05 g) was added to the $K_2Cr_2O_7$ solution (10 mL). The concentrations of the $K_2Cr_2O_7$ solution were set at 11.77, 16.17, 40.16, 74.66, and 98.33 mg/L, respectively. The solution was stirred at room temperature for 24 h until adsorption equilibrium was reached. The adsorbent was separated from the solution by centrifugation, and the concentration of the chromium solution was determined by inductively coupled plasma-optical emission spectrometry (ICP-OES).

### 2.5. Dehydrogenation of ethane coupled with reverse water–gas shift reaction

The equipment used for the dehydrogenation of ethane coupled with the reverse water–gas reaction is shown in Fig. 1. The mass of the catalyst was 0.1 g and the flow rate of the gas was 30 mL/min (carbon dioxide at 25 mL/min and ethane at 5 mL/min). The entire reaction system was maintained at atmospheric pressure. The reaction was performed in a stainless-steel tube with an inner diameter of 4 mm. The reactor was filled with quartz cotton, quartz sand (0.2 g, 20–40 mesh), 0.1 g catalyst, and quartz cotton in sequence from bottom to top. The activity of the catalyst was evaluated based on the ethylene yield. The composition and content of the reactants and products were analyzed using gas chromatography (FL-fl 9790II) with a KB-plot Q column. The

carrier gas and combustion gases were hydrogen and compressed air, respectively. First, the temperature of the reactor was heated to 650°C and $N_2$ was injected into the reactor. When the reactor temperature was stabilized, the nitrogen valve was closed. The carbon dioxide and ethane were fed into the reactor and reacted with each other.

### 2.6. Characterization of the catalyst

The valence states and elemental composition of the catalyst were determined using X-ray photoelectron spectroscopy (XPS; Thermo-Fisher Scientific, ESCALAB 250Xi). The crystal structure of the prepared $ZrO_2$ was characterized using an X-ray diffractometer (DX-2007 SSC). The variation in the morphology was observed using scanning electron microscopy (SEM, JSM-7500F). The photocurrent and cyclic voltammetry (CV) curves were obtained using an electrochemical workstation (Shanghai Chenhua, 760E). A field-emission transmission electron microscope (FEI, Tecnai G2 F20) was used to observe the lattice fringes of a-$ZrO_2$. The thermal stability of the deactivated catalyst was analyzed using thermogravimetry-differential scanning calorimetry (TG-DSC; STA449F3 Jupiter). The carbon deposited before and after the reaction was analyzed using Raman spectroscopy (Thermo Fisher Technologies Ltd., DXR microscope).

## 3. Result and discussion

### 3.1. Photocatalytic reduction of Cr(VI)

The adsorption ability of the catalysts without irradiation was tested, as presented in Table 1. The catalyst (0.1 g) was added to potassium dichromate solution with a (20.03 mg/L). In the absence of light, the concentration of Cr(VI) decreased from 20.03 to 0.4533 mg/L over 60 min. Under irradiation, the concentration of Cr(VI) decreased to 0.00032 mg/L. As a result, the prepared a-$ZrO_2$ exhibited photocatalytic reduction and Cr(VI) adsorption ability.

The presence of a sacrificial agent also plays an important role in the photocatalytic process, essentially impacting its efficiency. Herein, methanol was used as a sacrificial agent to investigate the effect of the sacrificial agent on photocatalytic efficiency. The variation in the Cr(VI) concentration in the solution with time is shown in Fig. 1. With 0.05 g methanol, the Cr(VI) reduction efficiency reached 100% in 10 min. When the dosage of the sacrificial agent was reduced to 0.025 g, the reduction efficiency reached 100% in 25 min. Without the sacrificial agent, the reaction time was extended to 51 min. Therefore, the addition of a sacrificial agent can accelerate the rate of Cr(VI) removal from the solution and decrease the reaction time.

The above-discussed experiments indicate that a-$ZrO_2$ has a large Cr(VI) adsorption capacity and strong photocatalytic ability. To determine the maximum amount of Cr(VI) that a-$ZrO_2$ can remove, it was mixed with an excess potassium dichromate solution. After the reaction, the composition of the Cr/a-$ZrO_2$ and the concentration of the solution were determined (Table 2). Cr was deposited on the a-$ZrO_2$ and only a small amount of Cr remained in the solution. The mass fraction of chromium on Cr/a-$ZrO_2$ was 5.012%.

The Cr/a-$ZrO_2$ retrieved after the photocatalytic reaction was analyzed using XPS to determine the valence state of Cr. The Cr on the surface was in the positive trivalent state (Fig. 2b). The corresponding binding energies were 586.3 and 576.6 eV. These binding energies match that of the chromium atoms in chromium oxide, which is consistent with ultraviolet–visible direct reflectance spectroscopy (UV-Vis DRS) data. The obtained Cr/a-$ZrO_2$ was further evaluated by high-resolution transmission electron microscopy (HRTEM) and selected area electron diffraction (SAED), as shown in Fig. 2c and d. Note that amorphous materials

Table 1
Cr(VI) concentration in solution in mg/L

| | |
|---|---|
| Initial concentration | 20.03 |
| Without light | 0.4533 |
| 30 min irradiation | 0.00032 |

Table 2
Concentration of Cr detected using inductively coupled plasma-optical emission spectrometry (ICP-OES) in mg/L

| | |
|---|---|
| 1st group | 0.00016 |
| 2nd group | 0.00022 |
| 3rd group | 0.00091 |
| Cr/a-$ZrO_2$ | 25.36 |

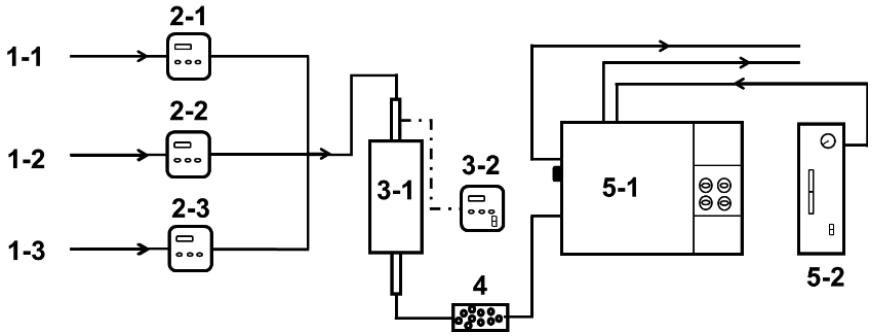


Fig. 1. Ethane dehydrogenation catalyst evaluation device. 1–1: carbon dioxide, 1–2: ethane, 1–3: nitrogen, 2–1 (2,3): mass flowmeter, 3–1: reactor, 3–2: thermocouple thermometer, 4: drying bottle, 5–1: gas chromatograph 5–2: high-purity hydrogen generator.

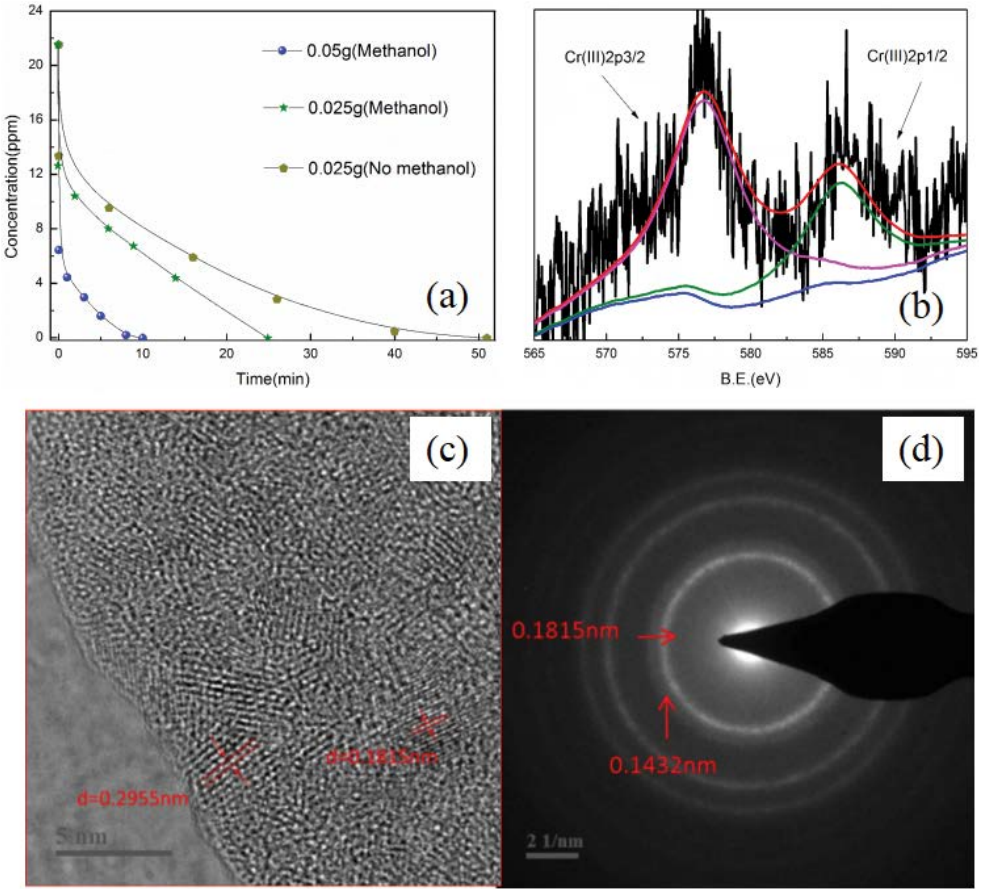


Fig. 2. (a) Concentration of Cr(VI) during the reaction, (b) X-ray photoelectron spectroscopy (XPS) analysis of chromium on Cr/a-$ZrO_2$ surface, (c) High-resolution transmission electron microscopy (HRTEM) analysis of Cr/a-$ZrO_2$, and (d) Selected area electron diffraction (SAED) analysis of Cr/a-$ZrO_2$.

are characterized by long-range disorder and short-range ordering. In Fig. 2d, the halo in the SAED pattern indicates that the atoms were arranged in a short-range order. In the HRTEM pattern, some local lattice fringes associated with short-range order were observed; however, the overall structure was amorphous. The lattice of the tetragonal zirconia 101 crystal plane, $d$ = 0.2955 nm, was observed in the HRTEM image. The above X-ray diffraction (XRD) results indicate that a-$ZrO_2$ is amorphous. Moreover, the lattice fringe of the Cr(0 2 4) crystal surface with $d$ = 0.1815 nm was also observed in the HRTEM image. Electron diffraction spots belonging to the $Cr_2O_3$ (3 0 0) crystal plane with $d$ = 0.1432 nm and crystal plane (0 2 4) with $d$ = 0.1815 nm were observed in the SAED pattern. Thus, the chromium deposited on a-$ZrO_2$ is chromium oxide.

### 3.2. Mechanism of adsorption and photocatalysis

These experiments demonstrated that a-$ZrO_2$ had a large capacity for Cr(VI) adsorption. The adsorption performance is closely related to the specific surface area. The surface area of a-$ZrO_2$, determined using the Brunauer–Emmett–Teller (BET) method, was 58.72 $m^2/g$. Therefore, the adsorption capacity of a-$ZrO_2$ was not determined by the specific surface area but may be related to the surface functional groups.

Table 3
Concentration of Cr determined using inductively coupled plasma-optical emission spectrometry (ICP-OES)

| Equilibrium concentration (mg/L) | Adsorption quantity (mg) |
|---|---|
| $1.79 \times 10^{-3}$ | $4.49 \times 10^{-2}$ |
| $2.327 \times 10^{-4}$ | $6.21 \times 10^{-2}$ |
| $2.28 \times 10^{-3}$ | $1.50 \times 10^{-1}$ |
| $2.56 \times 10^{-1}$ | $2.36 \times 10^{-1}$ |
| $5.21 \times 10^{-1}$ | $2.73 \times 10^{-1}$ |

Reportedly, $ZrO_2$ prepared via anodic oxidation exhibits a strong capacity for Cr(VI) adsorption owing to the abundant Zr-OH on the surface. In this study, a-$ZrO_2$ was obtained without annealing after the solvothermal treatment.

The adsorption kinetics are presented in Table 3. The above data were fitted to the Langmuir, Freundlich, and Redlich–Peterson models, respectively. The adsorption process was best described by the Redlich–Peterson models, with chi-square ($\chi^2$) equal to $4.6 \times 10^{-4}$ (Fig. 3). Therefore, the strong adsorption capacity of a-$ZrO_2$ was the result of both physical adsorption and chemical adsorption. The maximum adsorption capacity of the adsorbent was 14.46 mg/g.

For systems with solids and liquids, the dispersion of the adsorbent plays an important role in controlling the reaction rate. Therefore, the zeta-electric potential of a-$ZrO_2$ and s-$ZrO_2$ was determined (Table 4) to be 17.6 and 5.43 mV, respectively. Note that according to the relationship between the electrical potential and system stability, the system is prone to rapid condensation in the potential range of 0 to ±10 mV. The system is more stable in the zeta potential range from ±10 to ±30 mV. Therefore, the a-$ZrO_2$ particles were better dispersed in the solution, where this good dispersion had a positive impact on the reaction by reducing the penetration of light and increasing the absorption of light, reducing agglomeration, and exposing more reactive sites. Therefore, the good dispersion of a-$ZrO_2$ in the solution is one of the reasons for the high photo deposition rate of Cr(VI).

a-$ZrO_2$ has an excellent photocatalytic activity for the degradation of Cr(VI). To investigate the influence of the photoelectric effect, the generation of photoelectrons by a-$ZrO_2$ and s-$ZrO_2$ per unit of time was studied under the same conditions. The photocurrent generated by a-$ZrO_2$ and s-$ZrO_2$ under UV light was measured (Fig. 4). Evidently, under the same conditions, the photocurrent of a-$ZrO_2$ was approximately twice that of s-$ZrO_2$, which suggests that the number of photoelectrons produced by a-$ZrO_2$ that can effectively participate in the reduction reaction was greater than that produced by s-$ZrO_2$. Therefore, the rate of photocatalytic degradation of Cr deposition on a-$ZrO_2$ was faster than that on s-$ZrO_2$. This result comprehensively explains the effect of the quantum efficiency on the degradation rate of Cr(VI), where the photogenerated electrons are an influential factor.

The CV curves of a-$ZrO_2$ and s-$ZrO_2$ were acquired using the three-electrode system, with a saturated calomel electrode as the reference electrode, and 0.1 mol/L sodium sulfate and 20 mg/L potassium dichromate solution as the electrolyte. The results are shown in Fig. 4b. Evidently from the CV curve, the reduction initiation potentials of a-$ZrO_2$ and s-$ZrO_2$ were found to differ ($E_{red(a\text{-}ZrO_2)}$ = –0.99 V; $E_{red(s\text{-}ZrO_2)}$ = –1.44 V) when the voltage was decreased from 0 to –3 V.

The calculated LUMO energy level for a-$ZrO_2$ was $E_{LUMO} = E_{red(a\text{-}ZrO_2)}$ + 0.2415 V = –0.75 eV, and that for s-$ZrO_2$ was $E_{LUMO} = E_{red(a\text{-}ZrO_2)}$ + 0.2415 V = –1.1985 eV. The LUMO energy levels of both were less than the Cr(III)/Cr(0) reduction potential of –0.74 eV, which is consistent with the UV-Vis data for a-$ZrO_2$.

At the same voltage, the current of a-$ZrO_2$ was larger than that of s-$ZrO_2$, which indicates that the impedance of a-$ZrO_2$ is smaller than that of s-$ZrO_2$. This is more conducive to the transmission of electrons and the separation of photogenerated electrons and holes. Further, the recombination of photoelectrons and holes was reduced, and the probability of photoelectrons transmission to the semiconductor surface to participate in the reduction reaction was increased. This feature was also reflected in the photocurrent test. When irradiation was discontinued, the photocurrent generated by a-$ZrO_2$ dropped rapidly to nil, and the photocurrent of s-$ZrO_2$ decreased gradually. Therefore, the quantum efficiency of

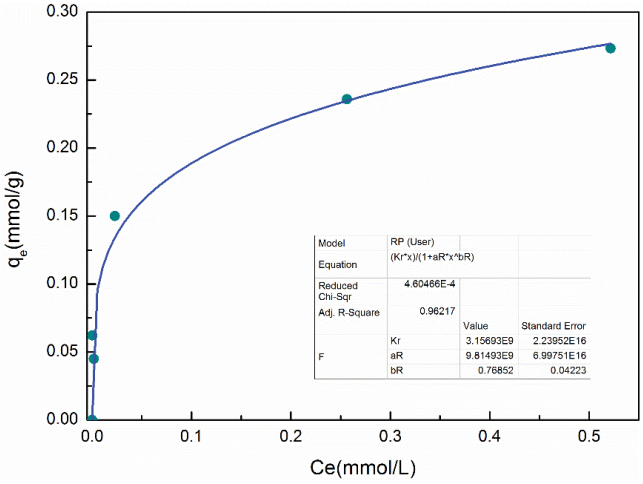


Fig. 3. Redlich–Peterson fitted absorption isotherms.

Table 4
Results of zeta potential

| Catalyst | First value | Second value | Third value | Average value |
|---|---|---|---|---|
| a-ZrO2 | –17.5 mV | –17.7 mV | –17.6 mV | –17.6 mV |
| s-$ZrO_2$ | –5.3 mV | –5.5 mV | –17.6 mV | –5.43 mV |

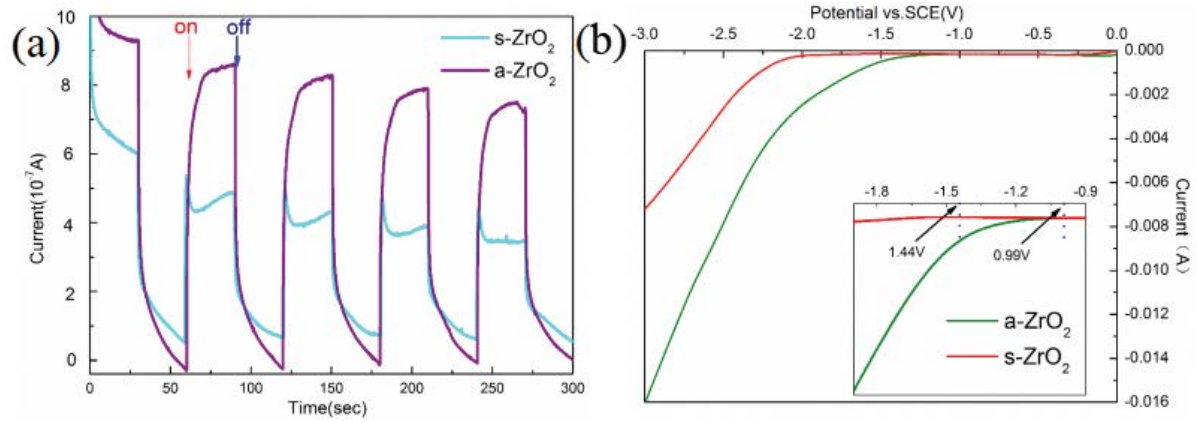


Fig. 4. (a) Photocurrent of a-$ZrO_2$ and s-$ZrO_2$, and (b) cyclic voltammetry (CV) curve of a-$ZrO_2$ and s-$ZrO_2$.

a-$ZrO_2$ is high, which is conducive to accelerating the photocatalytic reaction.

### 3.3. Catalysis of Cr/a-$ZrO_2$ ethane dehydrogenation coupled with reverse water gas reaction

To confirm that chromium in the by-product Cr/a-$ZrO_2$ can catalyze the ethane dehydrogenation coupled reverse water gas reaction and to evaluate the deactivation characteristics of the catalyst, eight groups of experiments were performed. Fresh a-$ZrO_2$, and by-product Cr/a-$ZrO_2$ were used in the experiments to prove the catalytic effect of chromium. Potassium dichromate solutions (20 mL) with concentrations of 20 and 30 mg/L were individually added to a quartz tube containing fresh a-$ZrO_2$ (0.1 g), respectively. After reacting for 3 h under UV light, the solid by-products were separated and labeled as $Cr^1_{20}$/a-$ZrO_2$ and $Cr^1_{30}$/a-$ZrO_2$, respectively, and the catalyst numbers for the second and third regenerations were analogous.

In the one-step comprehensive utilization process, a-$ZrO_2$ exhibited good adsorption and photodegradation performances. To further illustrate that a-$ZrO_2$ is suitable for this process and has a good catalytic performance, ethane dehydrogenation coupled with a reverse water gas reaction was catalyzed using the by-product Cr/a-$ZrO_2$. The ethylene yield from the catalytic reaction is shown in Fig. 5. The reactivity of fresh a-$ZrO_2$ was very low (2%), whereas the catalytic activities of $Cr_{20}$/a-$ZrO_2$ and $Cr_{30}$/a-$ZrO_2$ after photocatalytic deposition of chromium were significantly improved compared with that of fresh a-$ZrO_2$. The maximum ethylene yields reached 11.8% and 12.9%, respectively, thus indicating that the surface chromium in the by-product plays a significant catalytic role.

The maximum ethylene yield of $Cr_{30}$/a-$ZrO_2$ was 1.1% higher than that of $Cr_{20}$/a-$ZrO_2$, which indicates that the greater the loading amount of Cr, the better the catalytic activity of the catalyst. $Cr_{30}$/a-$ZrO_2$ was deactivated faster than $Cr_{20}$/a-$ZrO_2$, which may be due to the greater chromium loading: the faster the reaction, the faster the catalyst deactivation. Due to the rapid deactivation of the catalyst, its service life was studied. The highest yield (30%) in the ethylene yield time curve was selected as the deactivation time point for the catalyst (Fig. 5b). The service life of the $Cr_{20}$/a-$ZrO_2$ and $Cr_{30}$/a-$ZrO_2$ catalysts was 160 and 130 min, respectively. Thus, the greater the chromium load, the faster the catalyst deactivation, and the shorter the service life of the catalyst. The service life of the regenerated catalyst did not differ from that of the fresh catalyst, thus indicating that the catalyst can be effectively regenerated and that deactivation may be caused by carbon deposition.

To prove that the deactivation of the by-product Cr/a-$ZrO_2$ is caused by carbon deposition, the catalyst was characterized before and after ethane dehydrogenation coupled with the reverse water gas reaction and after regeneration using SEM. The results are shown in Fig. 6. At a magnification of 15 K, numerous small, disordered holes were observed on the surface of non-deactivated Cr/a-$ZrO_2$. The deactivated Cr/a-$ZrO_2$ was different from the non-deactivated Cr/a-$ZrO_2$. The particles were no longer clear and agglomerated, which is caused by the accumulation of small broken particles produced by carbon deposition, and new substances were generated on the surface of deactivated Cr/a-$ZrO_2$. After roasting, the crystalline substances on the surface of Cr/a-$ZrO_2$ disappeared, and the surface returned to a disordered state. The deactivated catalyst was subjected to thermogravimetric analysis (TG) and differential scanning calorimetry (DSC). The results exhibit that the weight loss of the catalyst began at 300°C (Fig. 7a and b), and a distinct exothermic peak at 320°C was observed in the DSC curve, which was derived from the carbon deposition during ethane dehydrogenation.

Unused Cr/a-$ZrO_2$ and deactivated Cr/a-$ZrO_2$ were characterized by Raman spectroscopy. It was determined that the deactivation was caused by carbon deposition given the presence of a carbon peak in the Raman spectrum of the surface of the deactivated catalyst. As shown in Fig. 7b, two distinct carbon peaks at 1,360 and 1,600 $cm^{-1}$ appeared in the spectrum of the deactivated catalyst after the reaction attributed to the D peak of the defect graphite crystal and the G peak of graphite crystal, respectively. The G peak was caused by the tensile vibration of the $sp^2$ hybrid carbon atoms in the

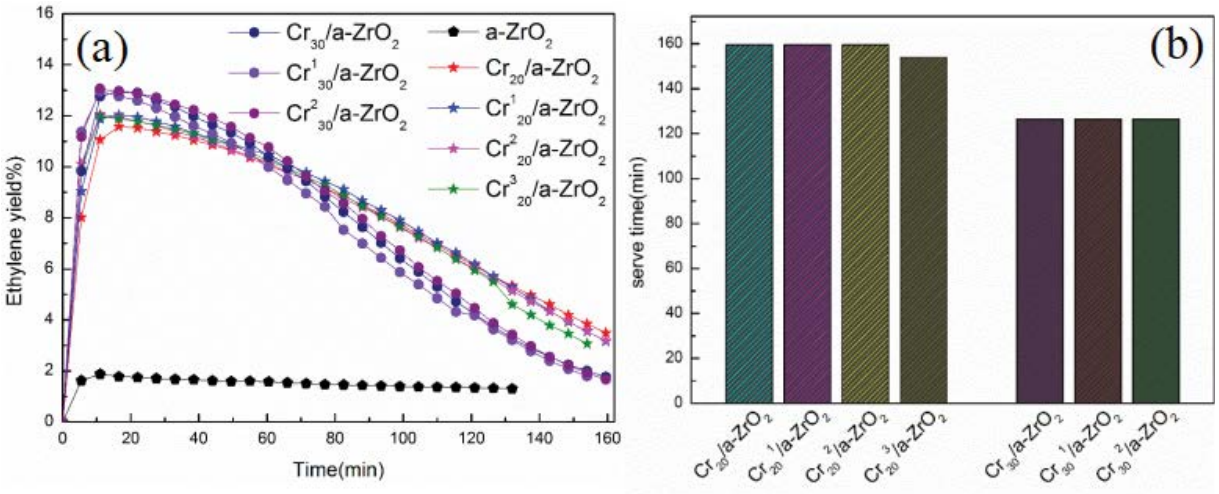


Fig. 5. (a) Ethylene yield, and (b) lifetime of different catalysts.

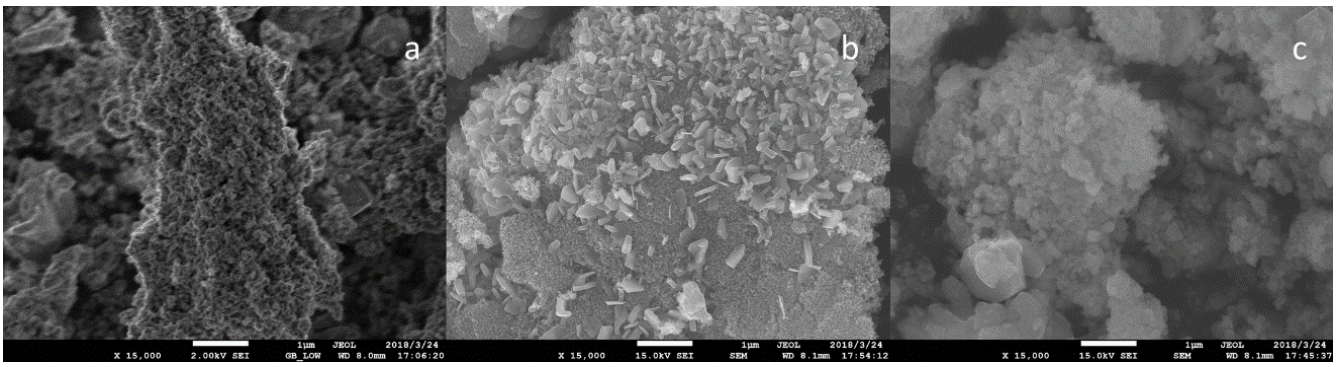


Fig. 6. Scanning electron microscopy (SEM) images of (a) Cr/a-$ZrO_2$, (b) deactivated Cr/a-$ZrO_2$, and (c) Cr/a-$ZrO_2$ after regeneration.

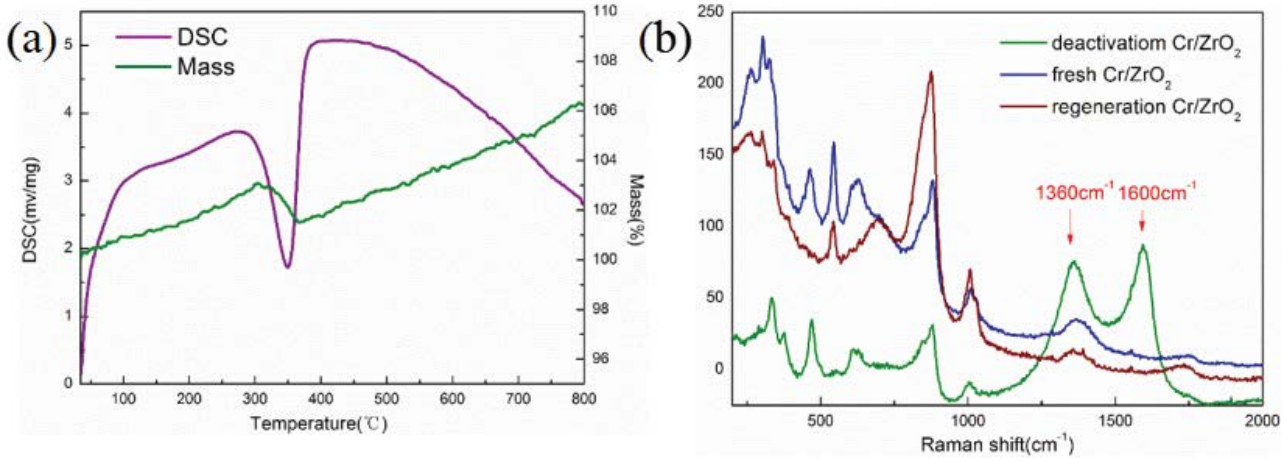


Fig. 7. (a) Thermogravimetric analysis and differential scanning calorimetry (TG-DSC) analysis of deactivated catalyst and (b) Raman spectra of catalyst.

graphite layer, which reflects the symmetry and order of the graphitic carbon, whereas the D peak was caused by the lattice vibration leaving the Brillouin region, which corresponds to the respiratory vibration of the six-membered ring of $sp^3$ hybrid carbon atoms, which is used to characterize the edge and in-plane defects of the grain boundaries. In the Raman spectrum of the deactivated catalyst, the G peak had a high intensity and narrow half-peak width, whereas the D peak was broad, which indicates that the degree of carbon deposition and graphitization on the catalyst surface was high, and numerous defects composed of graphite crystals and amorphous carbon were observed. This conclusion is supported by the SEM results shown in Fig. 8. The D and G peaks of carbon in the Raman spectra of Cr/a-$ZrO_2$ regenerated by calcination disappeared, thus confirming that the deactivation of the catalyst was indeed caused by carbon deposition.

### 3.4. Performance of other photocatalysts

To investigate the effect of the type of photocatalyst, six photocatalysts with wide bandwidths and small conduction potentials, namely β-$Ga_2O_3$, $La_2O_3$, $SrTiO_5$, MnO, SnO, and s-$ZrO_2$, were evaluated. Fig. 9a shows that the fresh s-$ZrO_2$ consisted of a mixture of monoclinic phase (PDF #37-1484) and tetragonal phase (PDF #50-1089) crystals. The XRD spectrum of the post-reaction byproduct Cr/s-$ZrO_2$ was almost identical to that of the fresh s-$ZrO_2$, with no diffraction peaks appearing or disappearing because the chromium on s-$ZrO_2$ was present in the form of amorphous or highly dispersed particles.

Fig. 9b shows that the fresh β-$Ga_2O_3$ (before the reaction) belongs to the monoclinic system (PDF #41-1103) of gallium oxide and has high crystallinity. The XRD pattern of the post-reaction by-product Cr/β-$Ga_2O_3$ was almost identical to that of β-$Ga_2O_3$, with no new diffraction peaks and no disappearance of any diffraction peaks. The reaction had almost no effect on the main body of β-$Ga_2O_3$. Similarly, the XRD patterns of $La_2O_3$ were acquired before and after the photocatalytic degradation of Cr to observe the change in the phase before and after the reaction to study the loading on the surface of $La_2O_3$ (Fig. 9c). The XRD data for $La_2O_3$ before the reaction showed that it corresponded to the hexagonal crystalline phase (PDF #05-0602) with good crystallinity and no diffraction peaks of other impurities. The XRD results of the by-product Cr/$La_2O_3$ after the lanthanum oxide photoreaction indicated the conversion of lanthanum oxide owing to the conversion of rare earth metal oxides to hydroxide in the presence of moisture or water.

When the catalyst was loaded on the surface to a certain level and crystals were produced, the XRD spectra of $SrTiO_3$

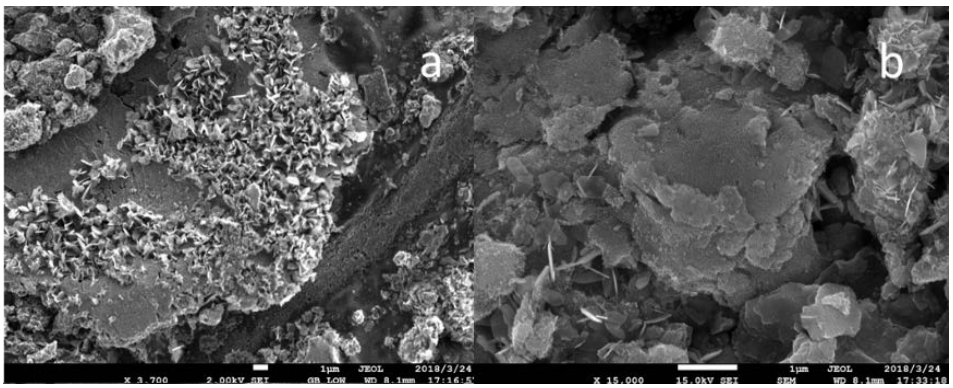


Fig. 8. Scanning electron microscopy (SEM) images of carbon deposited on the catalyst.

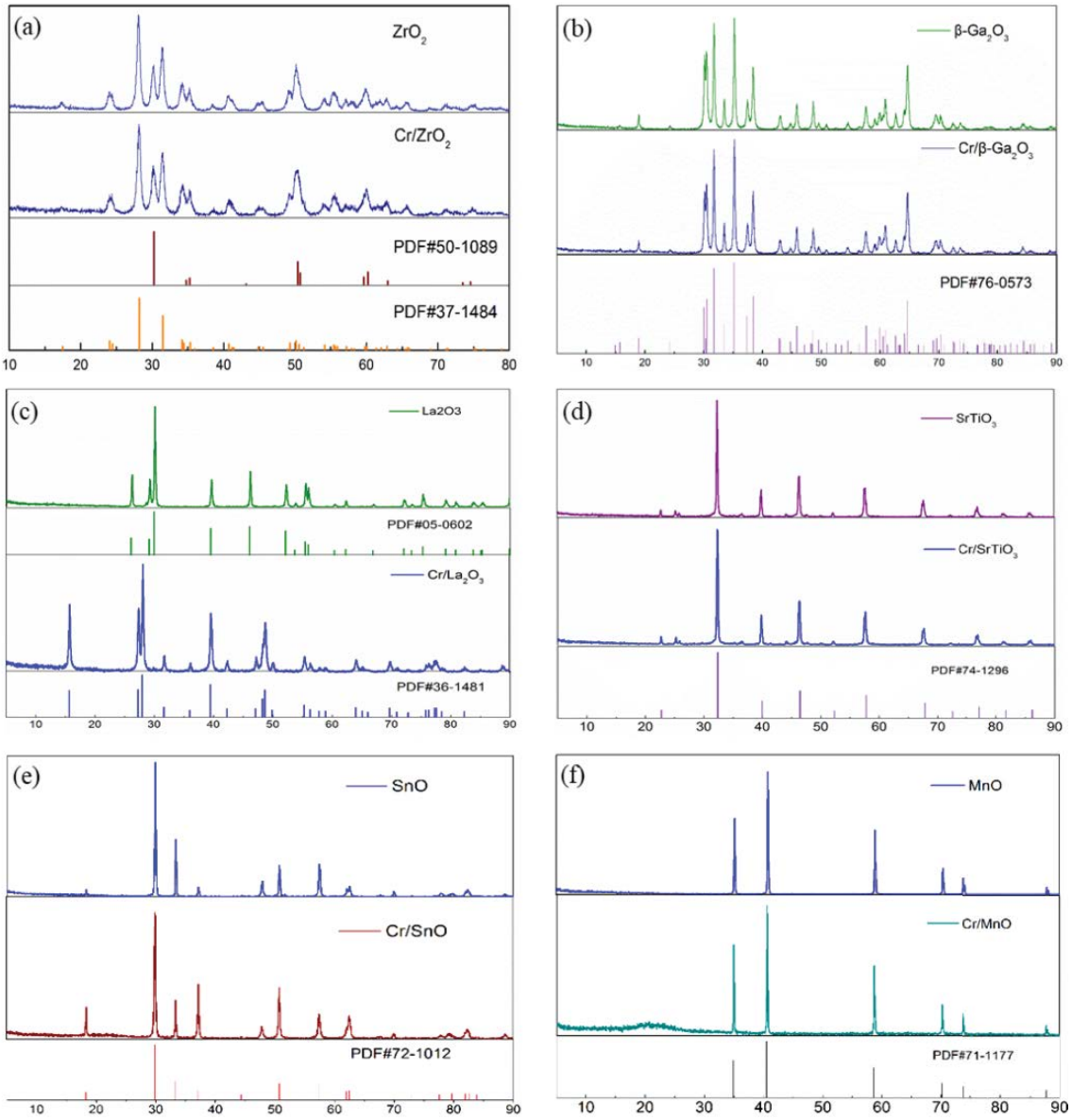


Fig. 9. X-ray diffraction (XRD) patterns of (a) $ZrO_2$ before and after photocatalysis, (b) β-$Ga_2O_3$ before and after photocatalysis, (c) $La_2O_3$ before and after photocatalysis, (d) $SrTiO_3$ before and after photocatalysis, (e) Cr/SnO before and after photocatalysis, and (f) Cr/MnO before and after photocatalysis.

and Cr/$SrTiO_3$ diverged. The primary diffraction peaks of $SrTiO_3$ did not change during the reaction process (Fig. 9d), and the XRD spectra of $SrTiO_3$ and Cr/$SrTiO_3$ were nearly identical to those of the by-product Cr/$SrTiO_3$. This suggests that the catalyst was stable during the reaction process. The primary diffraction peaks of fresh SnO correspond to the tetragonal phase (PDF #72-1012). After the photocatalytic reaction, the positions of these peaks remained unchanged. Because no chromium peaks were detected on the surface, the Cr content was minimal with a highly scattered dispersion (Fig. 9e), which suggests that SnO is rather stable during the reaction process. MnO possessed high crystallinity and belonged to the cubic phase (PDF #72-1012), and lacked any additional impurity peaks. Fig. 9f demonstrates that MnO was also stable because the major diffraction peaks of MnO did not change during the photocatalytic process, and no diffraction peaks of chromium element peaks were observed.

In Fig. 10, the concentration of $Cr_2O_7^{2-}$ in the reaction solution was analyzed as a function of the degradation time. Fig. 10a shows that the amount of potassium dichromate in the solution, with an initial concentration of 40 mg/L was reduced to 28.7 mg/L after dark adsorption, followed by the reaction under the light. The $Cr_2O_7^{2-}$ concentration in the solution was reduced to 0.13 mg/L within 90 min, and the degradation rate of $Cr_2O_7^{2-}$ reached 99.67%. At the end of the reaction, the concentration of Cr is determined using ICP-OES, and the final concentration of Cr in the solution was 1.1 mg/L. The rate of $Cr_2O_7^{2-}$ in the solution by β-$Ga_2O_3$ was examined, and Fig. 10b shows the change in the $Cr_2O_7^{2-}$ concentration overtime during the degradation process. With increasing time, the amount of $Cr_2O_7^{2-}$ ions in the solution decreased. Within 910 min, the concentration of $Cr_2O_7^{2-}$ in the solution dropped from 40 to 2.96 mg/L.

Fig. 10c shows a decrease in the $Cr_2O_7^{2-}$ concentration from 40.13 to 6.47 mg/L in the solution over 910 min. The concentration of $Cr_2O_7^{2-}$ increased rather than decreased after dark adsorption. The concentration of $Cr_2O_7^{2-}$ in the solution of $SrTiO_3$ increased from 40.13 to 64.83 mg/L, and then declined to 5.13 mg/L within 910 min (Fig. 10d). Therefore, β-$Ga_2O_3$, $La_2O_3$, $SrTiO_3$, MnO, and SnO affect the photocatalytic degradation of chromium. However, the degradation rate was much different from that obtained with $ZrO_2$. Moreover, the concentration of $Cr_2O_7^{2-}$ in the solution decreased from 36.5 to 17.5 and 22 mg/L after 910 min during the degradation of $Cr_2O_7^{2-}$ in the solution by SnO and MnO. The degradation rate and post-degradation concentration of the solution using SnO and MnO were very poor compared with those of the other substances (Fig. 10e and f).

As demonstrated in Fig. S1, there is no discernible interaction between $ZrO_2$ and the loaded Cr that was determined based on the UV-Vis DRS profiles and calculation of prohibited bandwidth before and after the reaction over $ZrO_2$. Excitation of the d-d electron leap of the octahedrally coordinated $Cr^{3+}$ cation was responsible for the additional absorption bands at 377.5 nm and 600 nm in the Cr/$ZrO_2$ spectra. To construct the ethylene yield-time curve depicted in Fig. 11a, the ethane dehydrogenation, and inverse water gas reactions were catalyzed using the by-product Cr/$ZrO_2$ in a fixed-bed reactor. The fresh $ZrO_2$ had almost no catalytic activity and the maximum yield reached only 2.1%, whereas the highest ethylene yield of the by-product Cr/$ZrO_2$ reaches 13.37%. The data indicated that the Cr on the surface of Cr/$ZrO_2$ plays a catalytic role, thus resulting in an experimental Cr/$ZrO_2$ catalyst lifetime of 125 min. Fig. 11b demonstrates that the fresh β-$Ga_2O_3$ was also active with a yield of 9%; however, it underwent rapid deactivation of the

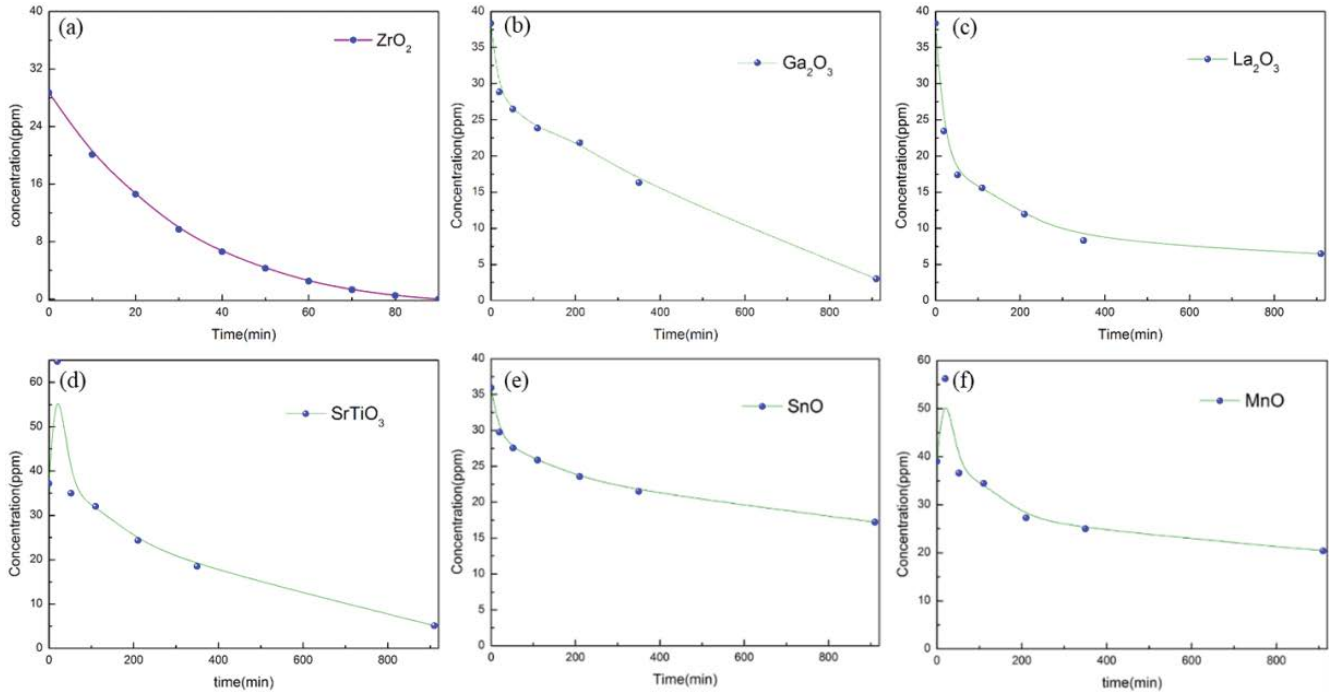


Fig. 10. $Cr_2O_7^{2-}$ concentration in the reaction solution vs. the degradation time: (a) $ZrO_2$, (b) $Ga_2O_3$, (c) $La_2O_3$, (d) $SrTiO_3$, (e) SnO, and (f) MnO.

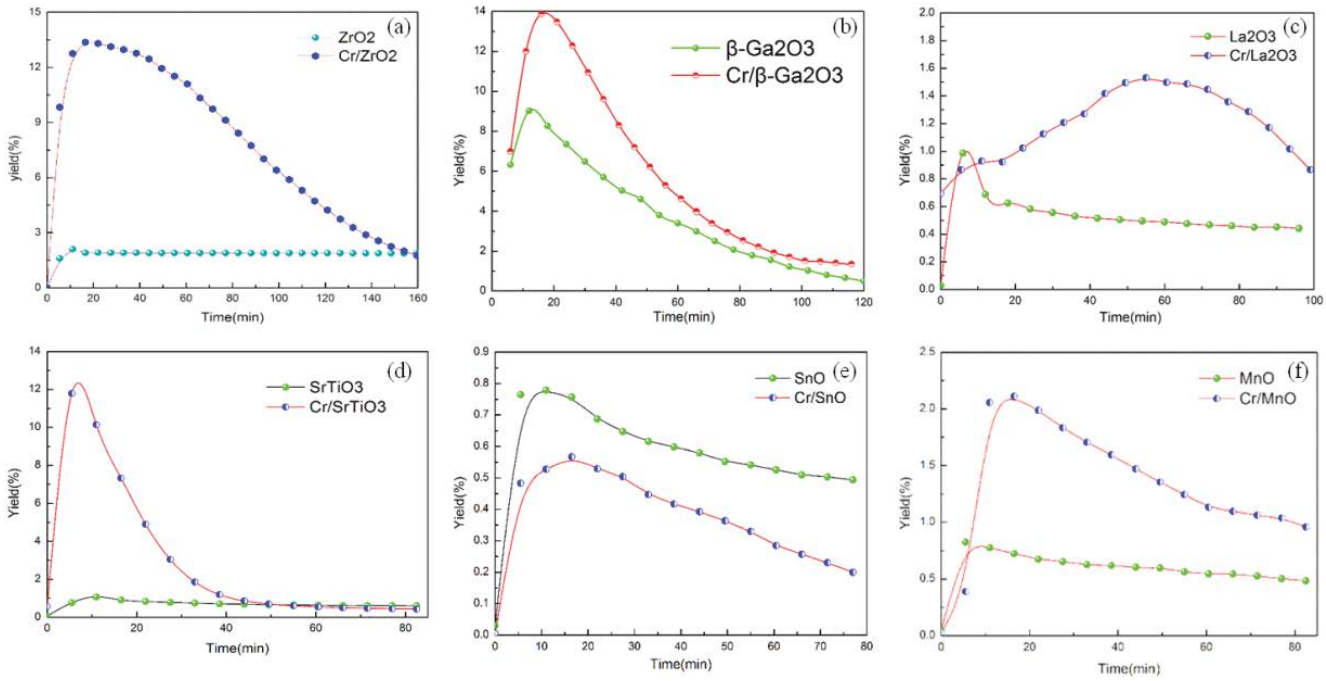


Fig. 11. Ethylene yield curve: (a) $ZrO_2$, (b) β-$Ga_2O_3$, (c) $La_2O_3$, (d) $SrTiO_5$, (e) MnO, and (f) SnO.

reactivity. Cr/β-$Ga_2O_3$ had a higher reactivity with a 14% ethylene yield, which is 55.6% higher than that of fresh β-$Ga_2O_3$. However, the latter was deactivated more rapidly. Taking the reaction process with a maximum ethylene yield of 30% as the deactivation time point, the lifetime of fresh β-$Ga_2O_3$ was 72 min and that of Cr/β-$Ga_2O_3$ was 65 min.

Because of the chromium loaded on the surface of β-$Ga_2O_3$, the catalyst had more surface acidic sites resulting in higher catalytic activity and deactivation rate. Fig. 11c shows a maximum $La_2O_3$ activity of only 1%, whereas Cr/$La_2O_3$ only increased the ethylene yield up to 1.6% compared with that obtained with fresh $La_2O_3$. The fresh strontium titanate had almost no catalytic activity with a maximum ethylene yield of only 1%, while the degradation by-product Cr/$SrTiO_3$ catalyzed the dehydrogenation of ethane with an ethylene yield of 12.1%, which is a significant enhancement. Thus, Cr on the surface of strontium titanate plays a catalytic role. Taking the reaction process with a maximum ethylene yield of 30% as the deactivation time point, the lifetime of the by-product Cr/$SrTiO_3$ was 28 min (Fig. 11d). This differed from the lifetime of the by-product zirconia catalyst, which may be owing to the presence of both acidic and basic sites on the surface of zirconia, and the mutual synergistic effect in the catalytic ethane dehydrogenation process, when Cr/SnO and Cr/MnO were used for the catalytic ethane dehydrogenation process (Fig. 11e and f). The catalytic activities of both SnO and Cr/SnO were low, with ethylene yields below 0.8%, respectively. This may be owing to the low Cr content on the surface of Cr/SnO, which leads to low reactivity. Therefore, the deficiency of the other materials compared with zirconia is primarily due to the slow degradation rate of the former materials, thus rendering them unsuitable for the dehydrogenation process.

## 4. Conclusion

In this work, amorphous $ZrO_2$ was prepared by a solvothermal method and used for the photocatalytic degradation of Cr(VI) in an aqueous solution. The prepared a-$ZrO_2$ considerably improved the degradation rate and degradation ability of Cr(VI), and the by-product had good catalytic activity for ethane dehydrogenation coupled with the reverse water gas reaction. The environmental-friendly comprehensive utilization of the amorphous a-$ZrO_2$ catalyst for the one-step photocatalytic reduction of Cr(VI), and exploitation of the by-product in catalytic ethane dehydrogenation coupled with the reverse water gas reaction was demonstrated to be feasible. To investigate the effect of the photocatalyst type, six photocatalysts with wide bandwidths and small conduction potentials were evaluated, and demonstrated that s-$ZrO_2$, β-$Ga_2O_3$, and $SrTiO_3$ are also effective for the photocatalytic degradation of Cr(VI) in wastewater. Among these catalysts, the s-$ZrO_2$ was determined to be the most promising one. This study provides a practical reference for the treatment of heavy metal ions and utilization of the by-products in wastewater, as well as for the removal of other metal ions.

## Declaration of competing interest

The authors declare that they have no known competing financial interests or personal relationships that could have appeared to influence the work reported in this study.

## Acknowledgments

This research was funded by Sinopec Northwest Oilfield Branch (21H0384). We would like to thank the Institute of New Energy and Low-Carbon Technology, Sichuan

University, for XRD and UV-Vis DRS analysis. Moreover, we are particularly grateful to the Center of Engineering Experimental Teaching, School of Chemical Engineering, Sichuan University, for the field emission transmission electron microscope by teacher Yanping Huang.

## References


[1] S. Bhero, E. Navara, Chemistry, Metallurgy and Mechanism of Microstructural Transformation in Hadfield Steel, High Chromium Cast Iron and Austempered Ductile Iron, 26th International Conference on Metallurgy and Materials (METAL), Brno, Czech Republic, 2017, pp. 117–125.

[2] Z.Q. Tan, U. Engstrom, K. Li, Y. Liu, Effect of furnace atmosphere on sintering process of chromium-containing steel via powder metallurgy, J. Iron Steel Res. Int., 28 (2021) 889–900.

[3] S. Toyai, K. Vilipornjaroen, Y. Pornputtkul, K. Piyamongkala, U. Kasetsart, Adsorption Chromium(VI) in Electroplating Wastewater by Chitosan Flakes, 48th Kasetsart University Annual Conference, Kasetsart Univ., Thailand, 2010, pp. 17–25.

[4] M.A.H. Geiger, L.F. Scheffel, C.L.P. Carone, F.D.P. Morisso, S.R. Kunst, J.Z. Ferreira, C.T. Oliveira, Evaluation of sputtering chromium coating as a electroplating substitute, Matéria, 25 (2020) 16, doi: 10.1590/S1517-707620200002.1054.

[5] S. Sundarapandiyan, P.E. Brutto, G. Siddhartha, R. Ramesh, B. Ramanaiah, P. Saravanan, A.B. Mandal, Enhancement of chromium uptake in tanning using oxazolidine, J. Hazard. Mater., 190 (2011) 802–809.

[6] I. Kabdasli, O. Tunay, E. Daymen, S. Meric, The factors affecting chromium precipitation in leather tanning industry wastewater, Fresenius Environ. Bull., 7 (1998) 859–866.

[7] C. Vancea, G. Mosoarca, A. Negrea, A. Latia, R.M. Jurca, New glass-ceramic matrix for the chromium wastes immobilization, Rev. Rom. Mater., 46 (2016) 296–302.

[8] R. Galindo, C. Gargori, N. Fas, M. Llusar, G. Monros, New chromium doped powellite (Cr-$CaMoO_4$) yellow ceramic pigment, Ceram. Int., 41 (2015) 6364–6372.

[9] M. Hubert, A.J. Faber, F. Akmaz, H. Sesigur, E. Alejandro, T. Maehara, S.R. Kahl, Stabilization of divalent chromium Cr(II) in soda-lime-silicate glasses, J. Non-Cryst. Solids, 403 (2014) 23–29.

[10] A. Basak, L. Ramrakhiani, S. Ghosh, R. Sen, A.K. Mandal, Preparation of chromium doped phosphate glass adopting microwave irradiation and comparative analysis of properties with conventional glass, J. Non-Cryst. Solids, 500 (2018) 11–17.

[11] X.R. Li, L.F. Jin, L. Huang, X.Y. Ge, H.Y. Deng, H.Y. Wang, Y.M. Li, L.Y. Chai, S.Q. Ma, Imidazolium-based cationic polymeric nanotraps for efficient removal of $Cr_2O_7^{2-}$, J. Environ. Chem. Eng., 9 (2021) 106357, doi: 10.1016/j.jece.2021.106357.

[12] E. Mourid, M. Lakraimi, L. Benaziz, High efficiency of calcined anionic clay to remove the chromate anions $CrO_4^{2-}$ from polluted water, French, 8 (2020) 26–47.

[13] H.K.S. Tan, Chromic acid removal by anion exchange, Can. J. Chem. Eng., 77 (1999) 143–149.

[14] N.N. Song, Y.B. Ma, The toxicity of $HCrO^{4-}$ and $CrO_4^{2-}$ to barley root elongation in solution culture: pH effect and modelling, Chemosphere, 171 (2017) 537–543.

[15] Y.F. Wang, H. Su, Y.L. Gu, X. Song, J.S. Zhao, Carcinogenicity of chromium and chemoprevention: a brief update, OncoTargets Ther., 10 (2017) 4065–4079.

[16] K.L. Ding, X.Y. Zhou, H. Hadiatullah, Y.L. Lu, G.Z. Zhao, S.R. Jia, R.F. Zhang, Y.P. Yao, Removal performance and mechanisms of toxic hexavalent chromium (Cr(VI)) with $ZnCl_2$ enhanced acidic vinegar residue biochar, J. Hazard. Mater., 420 (2021) 126551, doi: 10.1016/j.jhazmat.2021.126551.

[17] X.Z. Feng, Y.K. Zhang, C.Y. Liang, J.G. Yu, X.Y. Jiang, GO/PDDA/$Fe_3O_4$ nanocomposites used for instaneous Cr(VI) removal and a reliable direct filtration-adsorption application, Desal. Water Treat., 153 (2019) 145–156.

[18] C.S. Peng, H. Meng, S.X. Song, S. Lu, A. Lopez-Valdivieso, Elimination of Cr(VI) from electroplating wastewater by electrodialysis following chemical precipitation, Sep. Sci. Technol., 39 (2004) 1501–1517.

[19] O. Njoya, S.X. Zhao, Y.F. Qu, J.M. Shen, B.Y. Wang, H.Y. Shi, Z.L. Chen, Performance and potential mechanism of Cr(VI) reduction and subsequent Cr(III) precipitation using sodium borohydride driven by oxalate, J. Environ. Manage., 275 (2020) 111165, doi: 10.1016/j.jenvman.2020.111165.

[20] B.H. Xie, C. Shan, Z. Xu, X.C. Li, X.L. Zhang, J.J. Chen, B.C. Pan, One-step removal of Cr(VI) at alkaline pH by UV/sulfite process: reduction to Cr(III) and in situ Cr(III) precipitation, Chem. Eng. J., 308 (2017) 791–797.

[21] S.H. Qian, G.Q. Huang, J.S. Jiang, F. He, Y.T. Wang, Studies of adsorption behavior of crosslinked chitosan for Cr(VI), Se(VI), J. Appl. Polym. Sci., 77 (2000) 3216–3219.

[22] H.Z. Xie, Y.L. Wan, H. Chen, G.C. Xiong, L.Q. Wang, Q. Xu, X. Li, Q.H. Zhou, Cr(VI) adsorption from aqueous solution by UiO-66 modified corncob, Sustainability, 13 (2021) 12962, doi: 10.3390/su132312962.

[23] S. Edebali, E. Pehlivan, Removal of Cr(VI) from Aqueous Solutions by Ion Exchange-Microfiltration Hybrid Process, 2010 International Conference on Environmental Science and Development, World Acad Union-World Acad Press, Singapore, Singapore, 2010, pp. 243–247.

[24] Y.F. Ren, Y.H. Han, X.F. Lei, C. Lu, J. Liu, G.X. Zhang, B.L. Zhang, Q.Y. Zhang, A magnetic ion exchange resin with high efficiency of removing Cr(VI), Colloid Surf., A, 604 (2020) 125279, doi: 10.1016/j.colsurfa.2020.125279.

[25] A. Holda, E. Kisielowska, Biological removal of Cr(VI) ions from aqueous solutions by *Trichoderma viride*, Physicochem. Probl. Miner. Process., 49 (2013) 47–60.

[26] M. Sen, M.G. Dastidar, P.K. Roychoudhury, Biological removal of Cr(VI) using *Fusarium solani* in batch and continuous modes of operation, Enzyme Microb. Technol., 41 (2007) 51–56.

[27] S.Y. Li, Z.Q. Hu, S.B. Xie, H.Y. Liu, J.X. Liu, Removal of Cr(VI) from electroplating industry effluent via electrochemical reduction, Int. J. Electrochem. Sci., 13 (2018) 655–663.

[28] F.B. Yao, M.C. Jia, Q. Yang, K. Luo, F. Chen, Y. Zhong, L. He, Z.J. Pi, K.J. Hou, D.B. Wang, X.M. Li, Electrochemical Cr(VI) removal from aqueous media using titanium as anode: simultaneous indirect electrochemical reduction of Cr(VI) and *in-situ* precipitation of Cr(III), Chemosphere, 260 (2020) 127537, doi: 10.1016/j.chemosphere.2020.127537.

[29] H. Arslanoglu, H.S. Altundogan, F. Tumen, Photocatalytic reduction of Cr(VI) from aqueous solutions with formic acid in the presence of bauxite: kinetics and mechanism, Trans. Indian Inst. Met., 74 (2021) 3075–3084.

[30] C. Xu, P.F. Zhao, M. Cai, Z.G. Dan, S. Zeng, J.H. Du, P.Y. Yang, J. Xiong, Enhanced photocatalytic reduction of Cr(VI) by $Cu_2O/Bi_5O_7I$ microrods composites under visible light, J. Photochem. Photobiol., A, 395 (2020) 112495, doi: 10.1016/j.jphotochem.2020.112495.

[31] Q. Sun, H. Li, S.L. Zheng, Z.M. Sun, Characterizations of nano-$TiO_2$/diatomite composites and their photocatalytic reduction of aqueous Cr(VI), Appl. Surf. Sci., 311 (2014) 369–376.

[32] Y.C. Du, S.H. Zhang, J.S. Wang, J.S. Wu, H.X. Dai, $Nb_2O_5$ nanowires in-situ grown on carbon fiber: a high-efficiency material for the photocatalytic reduction of Cr(VI), J. Environ. Sci., 66 (2018) 358–367.

[33] X.W. Su, Z.H. Wang, Y. Huang, Z.Y. Miao, S.H. Wang, J.J. Wang, X.L. Zhang, X.M. Sun, H. Liu, Y.H. Sang, Triethanolamine interface modification of crystallized ZnO nanospheres enabling fast photocatalytic hazard-free treatment of Cr(VI) ions, Nanotechnol. Rev., 10 (2021) 847–856.

[34] J.K. Yang, S.M. Lee, M. Farrokhi, O. Giahi, M.S. Siboni, Photocatalytic removal of Cr(VI) with illuminated $TiO_2$, Desal. Water Treat., 46 (2012) 375–380.

[35] X.Q. Li, Z. Hong, S.Z. Kang, L.X. Qin, G.D. Li, J. Mu, Photocatalytic Degradation Activity of $TiO_2$ Nanotubes for Cr(VI), 3rd International Conference on Energy, Environment and Sustainable Development (EESD 2013), Trans Tech. Publications Ltd., Shanghai, Peoples R China, 2013, p. 715.

[36] B.Y. Zhang, G.H. Huang, M. Liu, D.M. Dong, B. Chen, W.C. Christine, ZnO-based solar photocatalysis for treatment

of Cr(VI) contamination, Trans. Nonferrous Met. Soc. China, 14 (2004) 49–53.
[37] Y. Xia, R.Q. Gang, L. Xu, S.J. Huang, L.X. Zhou, J. Wang, Nanorod-pillared mesoporous rGO/ZnO/Au hybrids for photocatalytic Cr(VI) reduction: enhanced Cr(VI) adsorption and solar energy harvest, Ceram. Int., 46 (2020) 1487–1493.
[38] C.S. Shen, H. Li, Y.Z. Wen, F. Zhao, Y.P. Zhang, D.L. Wu, Y.B. Liu, F. Li, Spherical $Cu_2O$-$Fe_3O_4$@chitosan bifunctional catalyst for coupled Cr-organic complex oxidation and Cr(VI) capture-reduction, Chem. Eng. J., 383 (2020) 123105, doi: 10.1016/j.cej.2019.123105.
[39] X.C. Dou, C.L. Zhang, H.F. Shi, The simultaneous promotion of Cr(VI) photoreduction and tetracycline removal over 3D/2D $Cu_2O$/BiOBr S-scheme nanostructures, Sep. Purif. Technol., 282 (2022) 120023, doi: 10.1016/j.seppur.2021.120023.
[40] W. Jiang, Q. Liu, Y. Tao, K.Q. Mu, Z. Wang, Y.M. Zhu, H.R. Yue, B. Liang, An environment-friendly strategy for one-step turning Cr(VI) contaminant into a Cr-loaded catalyst for $CO_2$ utilization, Adv. Sustain. Syst., 2 (2018) 1700165, doi: 10.1002/adsu.201700165.

## Supplementary information

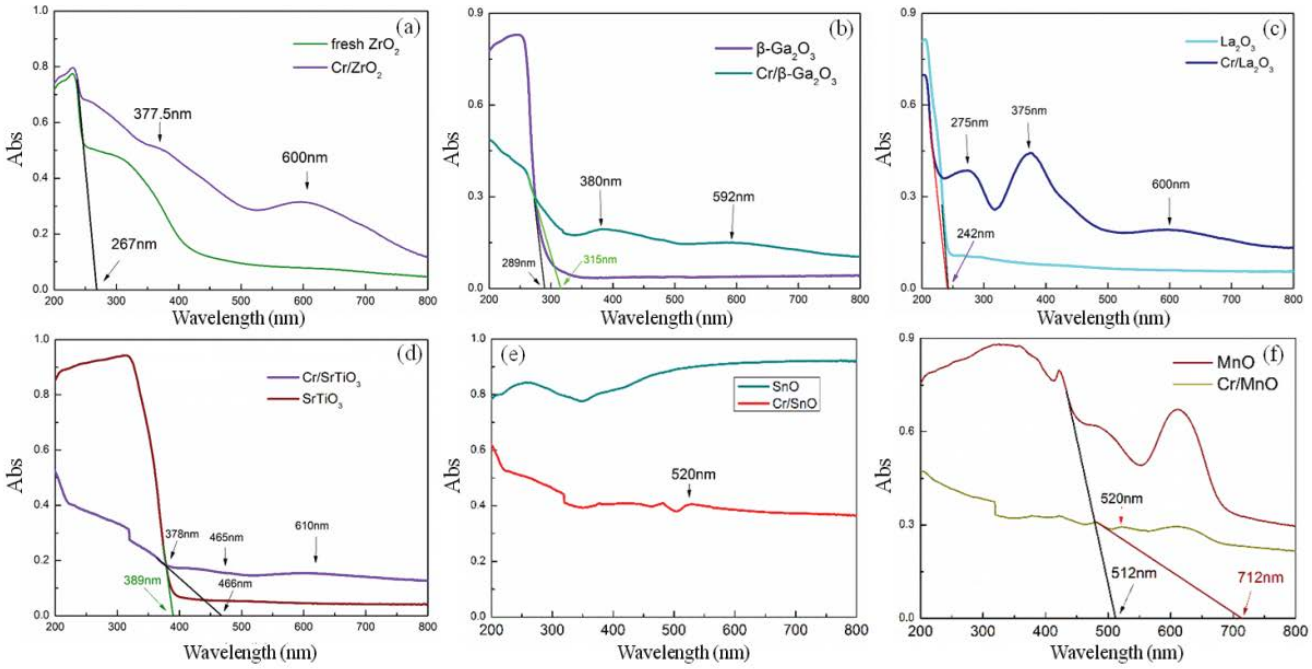


Fig. S1. Ultraviolet–visible direct reflectance spectroscopy (UV-Vis DRS): (a) fresh $ZrO_2$ and used $ZrO_2$, (b) fresh β-$Ga_2O_3$ and used β-$Ga_2O_3$, (c) fresh $La_2O_3$ and used $La_2O_3$, (d) fresh $SrTiO_3$ and used $SrTiO_3$, (e) SnO, and (f) MnO.